



Convolution quadrature time-domain boundary element method for 2-D and 3-D elastodynamic analyses in general anisotropic elastic solids



Akira Furukawa^{a,*}, Takahiro Saitoh^b, Sohichi Hirose^a

^a Department of Mechanical and Environmental Informatics, Graduate School of Information Science and Engineering, Tokyo Institute of Technology, 2-12-1, Ookayama, Meguro-ku, Tokyo 152-8552, Japan

^b Division of Environmental Engineering Science, Faculty of Science and Technology, Gunma University, 1-5-1, Tenjin, Kiryu, Gunma 376-8515, Japan

ARTICLE INFO

Article history:

Received 4 May 2013

Accepted 6 November 2013

Available online 28 November 2013

Keywords:

Boundary element method

Convolution quadrature method

General anisotropy

ABSTRACT

This paper presents a convolution quadrature time-domain boundary element method for 2-D and 3-D elastic wave propagation in general anisotropic solids. A boundary element method (BEM) has been developed as an effective and accurate numerical approach for wave propagation problems. However, a conventional time-domain BEM has a critical disadvantage; it produces unstable numerical solutions for a small time increment. To overcome this disadvantage, in this paper, a convolution quadrature method (CQM) is applied to the time-discretization of boundary integral equations in 2-D and 3-D general anisotropic solids. As numerical examples, the problems of elastic wave scattering by a cavity are solved to validate the present method.

© 2013 Elsevier Ltd. All rights reserved.

1. Introduction

A boundary element method (BEM) is known as an effective and accurate numerical approach for wave analysis, since a BEM requires boundary discretization only and is easily applicable to infinite or semi-infinite domains. A conventional time-domain BEM for elastodynamics has been developed by several researchers [4,8,13,18]. Although the transient BEM analysis requires time-domain fundamental solutions, such solutions cannot be found for some engineering problems, such as wave propagation in viscoelastic and fluid-saturated porous solids. In addition, the conventional time-domain BEM generates unstable numerical solutions unless a time increment is chosen adequately. Approaches for improving numerical stability have been proposed in the recent decade, e.g. the energetic wave formulation developed by Aimi and Diligenti [2], and a convolution quadrature time-domain BEM described below. Moreover, the BEM may also be unsuitable for large scale problems, because the method requires high computational costs to solve large scale problems. In the past few decades, the fast multipole BEM (FMBEM) has been developed for reducing required computational time and memory for various large scale problems. Alternatively, as a fast BEM in time-domain, the BEM accelerated by the plane wave time domain (PWTD) algorithm has been proposed [26]. However, the time-domain BEM still remains to be improved.

* Corresponding author. Tel.: +81 3 5734 3587.

E-mail address: furukawa.a.aa@m.titech.ac.jp (A. Furukawa).

Recently, a convolution quadrature time-domain BEM (CQ-BEM) was developed by Schanz and Antes [22]. The CQ-BEM uses a convolution quadrature method (CQM) for time-discretization in boundary integral equations. The CQM, proposed by Lubich [14–17], gives numerical approximation of convolution integrals. The approximation formula based on the linear multistep method using backward differential formula was derived firstly, and the Runge–Kutta based CQM was developed subsequently, with the aim of good performance in engineering applications [5]. This method is known to improve the numerical stability of a time-domain BEM. While a conventional time-domain BEM uses time-domain fundamental solutions, the CQ-BEM requires Laplace-domain ones. Therefore, the CQ-BEM can produce stable numerical solutions, even for a small time increment which is not allowed in a conventional time-domain BEM. In addition, the CQ-BEM can analyze wave propagation in viscoelastic solids [23] and fluid-saturated porous solids [24] for which time-domain fundamental solutions are not available. Because the fundamental solutions are expressed in the Laplace-domain, the CQ-BEM can be readily accelerated by implementing the FMM.

In some engineering fields, consideration of anisotropy is particularly important for wave analysis, and BEM has been applied to such kind of problems [3,6,7,19,20,25]. The BEM formulation for general anisotropic materials is much more complicated than isotropic formulations. For example, in wave analysis, Wang and Achenbach [30] derived time and frequency-domain fundamental solutions for general anisotropy based on the use of the Radon transform. Their fundamental solutions include surface integration over the unit sphere in 3-D problems and line integration over the unit circle in 2-D problems. A conventional

time-domain BEM for wave analysis in general anisotropic elastic solids has been developed by Wang et al. [31]. They solved wave scattering problems by a cavity in anisotropic solids. A conventional time-domain BEM, using traction BIEs, has also been applied to dynamic crack analyses in anisotropic solids [27,32]. Recently, elastic waves in general anisotropic elastic solids have been analyzed by the CQ-BEM [9,10,33], but in 2-D crack problems only.

In this paper, the formulation of a CQ-BEM for 2-D and 3-D general anisotropic solids is presented, and the validity of our proposed method is numerically tested. Note that the proposed formulation is based on the CQM with respect to the linear multistep method using backward differential formula. Parallel computing techniques, such as OpenMP, and MPI (Message Passing Interface) are utilized for numerical computations.

2. Problem statement

In this paper, a Latin suffix takes the values 1, 2 and 3, and a Greek suffix takes the values 1 and 2 only, unless otherwise stated. In addition, summation convention is valid for repeated indices throughout this paper.

Let us consider a wave scattering problem in an infinite, homogeneous, and linear anisotropic elastic solid V as shown in Fig. 1. If the scatterer's boundary in the solid V is represented as $S(S = S_1 \cup S_2, S_1 \cap S_2 = \emptyset)$, with the unit outward normal vector \mathbf{n} , the equations of motion at point \mathbf{x} and time t are given as follows:

$$\sigma_{ij,j}(\mathbf{x}, t) + \rho b_i(\mathbf{x}, t) = \rho \ddot{u}_i(\mathbf{x}, t) \tag{1}$$

where $\sigma_{ij}(\mathbf{x}, t)$ and $u_i(\mathbf{x}, t)$ represent the stress and displacement components, respectively. In addition, $b_i(\mathbf{x}, t)$ represents the body force component, and ρ is the density of the solid V . The dot notation shows differentiation with respect to time t , and the symbol $(\cdot)_{,i}$ represents the partial derivative with respect to x_i . According to linear elasticity theory, the stress-strain relation is expressed as follows:

$$\sigma_{ij}(\mathbf{x}, t) = C_{ijkl} \epsilon_{kl}(\mathbf{x}, t) \tag{2}$$

where C_{ijkl} is the fourth order elastic tensor of the solid V , and $\epsilon_{kl}(\mathbf{x}, t)$ represents the strain component expressed as follows:

$$\epsilon_{kl}(\mathbf{x}, t) = \frac{1}{2} \{ u_{k,l}(\mathbf{x}, t) + u_{l,k}(\mathbf{x}, t) \}. \tag{3}$$

The stress-strain relation as shown in Eq. (2) can be also expressed using the following contracted notation known as the Voigt notation [28]:

$$\sigma_I(\mathbf{x}, t) = C_{IJ} \epsilon_J(\mathbf{x}, t) \quad (I, J = 1, 2, \dots, 6). \tag{4}$$

In Eq. (4), the strain component $\epsilon_J(\mathbf{x}, t)$ is defined as

$$\epsilon_1 = \epsilon_{11}, \quad \epsilon_2 = \epsilon_{22}, \quad \epsilon_3 = \epsilon_{33}, \quad \epsilon_4 = 2\epsilon_{23}, \quad \epsilon_5 = 2\epsilon_{13}, \quad \epsilon_6 = 2\epsilon_{12}. \tag{5}$$

Moreover, the fourth order elastic tensor C_{ijkl} is related to the tensor C_{IJ} expressed in the Voigt notation in Eq. (4) by

$$I = \begin{cases} i & : i = j, \\ 9 - (i + j) & : i \neq j, \end{cases} \tag{6}$$

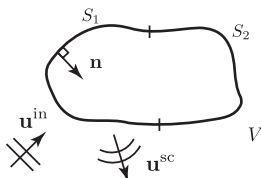


Fig. 1. An infinite, homogeneous, anisotropic solid with a cavity.

$$J = \begin{cases} k & : k = l, \\ 9 - (k + l) & : k \neq l. \end{cases} \tag{7}$$

Eqs. (6) and (7) yield the following associations: if $IJ = 1, 2$ or 3 , the stress and strain components in Eq. (4) correspond to axial components. On the other hand, if $IJ = 4, 5$ or 6 , they correspond to the shear components.

The total wave field $u_i(\mathbf{x}, t)$ can be expressed by the superposition of the incident and scattered wave fields represented by $u_i^{in}(\mathbf{x}, t)$ and $u_i^{sc}(\mathbf{x}, t)$, respectively, as follows:

$$u_i(\mathbf{x}, t) = u_i^{in}(\mathbf{x}, t) + u_i^{sc}(\mathbf{x}, t). \tag{8}$$

Moreover, the initial and boundary conditions are given as follows:

$$u_i(\mathbf{x}, t) = \dot{u}_i(\mathbf{x}, t) = 0, \quad t = 0, \tag{9}$$

$$u_i(\mathbf{x}, t) = u_i^*(\mathbf{x}, t), \quad \mathbf{x} \in S_1, \tag{10}$$

$$t_i(\mathbf{x}, t) = t_i^*(\mathbf{x}, t), \quad \mathbf{x} \in S_2, \tag{11}$$

where $t_i(\mathbf{x}, t)$ is the traction component expressed as follows:

$$t_i(\mathbf{x}, t) = \sigma_{ij}(\mathbf{x}, t) n_j(\mathbf{x}) = C_{ijkl} n_j(\mathbf{x}) u_{k,l}(\mathbf{x}, t). \tag{12}$$

In addition, $u_i^*(\mathbf{x}, t)$ and $t_i^*(\mathbf{x}, t)$ denote the prescribed values on boundaries S_1 and S_2 , respectively.

3. Convolution quadrature time-domain boundary element method (CQ-BEM)

3.1. Time-domain BEM formulation

For the exterior problem as shown in Fig. 1, the time-domain BIEs derived from the Betty-Rayleigh reciprocal theorem are expressed as

$$\epsilon(\mathbf{x}) u_i(\mathbf{x}, t) = u_i^{in}(\mathbf{x}, t) + \int_S U_{ij}(\mathbf{x}, \mathbf{y}, t) * t_j(\mathbf{y}, t) dS(\mathbf{y}) - \int_S W_{ij}(\mathbf{x}, \mathbf{y}, t) * u_j(\mathbf{y}, t) dS(\mathbf{y}) \tag{13}$$

where $U_{ij}(\mathbf{x}, \mathbf{y}, t)$ and $W_{ij}(\mathbf{x}, \mathbf{y}, t)$ represent displacement and traction fundamental solutions in time-domain, respectively. In addition, $\epsilon(\mathbf{x})$ is the free term [11], which depends on the shape of the boundary. If a piecewise constant boundary element approximation for spatial discretization is considered, $\epsilon(\mathbf{x})$ becomes

$$\epsilon(\mathbf{x}) = \begin{cases} 1 & : \mathbf{x} \in V \\ 1/2 & : \mathbf{x} \in S \\ 0 & : \text{otherwise.} \end{cases} \tag{14}$$

It is obvious that the presented formulation can treat domains with edges and corners, when the edge of boundary elements coincides with the corners. However, this formulation may not be adequate to analyze the domain with sharp corner, such as crack. In Eq. (13), $*$ denotes the Riemann convolution, defined as

$$f(t) * g(t) = \int_0^t f(t - \tau) g(\tau) d\tau. \tag{15}$$

Normally, the BIEs given by Eq. (13) can be directly discretized in time-domain. However, as mentioned before, this time discretization sometimes causes numerical instability. Therefore, in the following section, time-discretization procedure using the CQM is introduced to overcome the difficulty.

3.2. Discretization of time-domain BIEs using the CQM

The CQM, proposed by Lubich [14–17], provides numerical approximation of the convolution integral defined in Eq. (15) and improves numerical stability in the time stepping procedure.

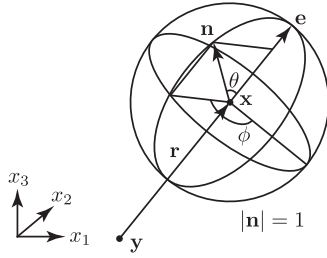


Fig. 2. Numerical integration over the unit sphere.

The CQM approximates the convolution defined in Eq. (15), as follows:

$$f(n\Delta t)*g(n\Delta t) = \sum_{k=0}^n \omega_{n-k}(\Delta t)g(k\Delta t) \quad (16)$$

where Δt is the time increment and $\omega_k(\Delta t)$ represents quadrature weights. The quadrature weights $\omega_k(\Delta t)$ with error magnitude $O(\epsilon)$ are determined by the Laplace transform of the function $f(t)$ and a linear multistep method as follows:

$$\omega_m(\Delta t) = \frac{1}{2\pi i} \int_{|z|=\mathcal{R}} \hat{f}\left(\frac{\gamma(z)}{\Delta t}\right) z^{-m-1} dz \quad (17)$$

where \hat{f} represents the Laplace transform. Moreover, the quadrature weight as shown in Eq. (17) can be approximated numerically, using the L -point trapezoidal rule as follows:

$$\omega_m(\Delta t) = \frac{\mathcal{R}^{-m} L^{-1}}{L} \sum_{l=0}^{L-1} \hat{f}\left(\frac{\gamma(z_l)}{\Delta t}\right) e^{-2\pi i m l/L} \quad (18)$$

where i is the imaginary unit, and \mathcal{R} is a CQM parameter given by

$$\mathcal{R} = \epsilon^{1/2L}. \quad (19)$$

In addition, $\gamma(z_l)$ represents the quotient of generating polynomials, which can be written as

$$\gamma(z_l) = \sum_{i=1}^k \frac{1}{i} (1-z_l)^i, \quad z_l = \mathcal{R} e^{-2\pi i l/L}. \quad (20)$$

Note that Eq. (20) corresponds to a backward differential formula of order k . In practical applications, first or second order backward differential formulas should be used in Eq. (20) to ensure high precision solutions.

Now, the CQM is applied to the time-discretization of Eq. (13). Dividing the boundary S into boundary elements and assuming the piecewise constant approximation, the discretized time-domain BIEs are derived as follows:

$$\frac{1}{2} u_{M,i}^{(n)} = u_{M,i}^{\text{in}(n)} + \sum_{k=1}^n \sum_{N=1}^{N_e} [A_{MN,ij}^{(n-k)} t_{N,j}^{(k)} - B_{MN,ij}^{(n-k)} u_{N,j}^{(k)}], \quad (\mathbf{x} \in S, M = 1, 2, \dots, N_e, n = 1, 2, \dots, N_t) \quad (21)$$

where N_e and N_t represent the number of boundary elements and total time steps, respectively. In addition, $A_{MN,ij}^{(m)}$ and $B_{MN,ij}^{(m)}$ are influence functions expressed as follows:

$$A_{MN,ij}^{(m)} = \frac{\mathcal{R}^{-m} L^{-1}}{L} \sum_{l=0}^{L-1} \left[\int_{S^N} \hat{U}_{ij}(\mathbf{x}^M, \mathbf{y}, s_l) dS(\mathbf{y}) \right] e^{-2\pi i m l/L}, \quad (22)$$

$$B_{MN,ij}^{(m)} = \frac{\mathcal{R}^{-m} L^{-1}}{L} \sum_{l=0}^{L-1} \left[\int_{S^N} \hat{W}_{ij}(\mathbf{x}^M, \mathbf{y}, s_l) dS(\mathbf{y}) \right] e^{-2\pi i m l/L} \quad (23)$$

where $s_l = \gamma(z_l)/\Delta t$. From Eqs. (22) and (23), it can be observed that the influence functions $A_{MN,ij}^{(m)}$ and $B_{MN,ij}^{(m)}$ include Laplace-domain displacement and traction fundamental solutions, $\hat{U}_{ij}(\mathbf{x}, \mathbf{y}, s)$ and $\hat{W}_{ij}(\mathbf{x}, \mathbf{y}, s)$, respectively.

3.3. Laplace-domain fundamental solutions for general anisotropic solid

As shown in Eqs. (22) and (23), Laplace-domain fundamental solutions are required to compute the influence functions. In this research, these fundamental solutions for elastic solids of general anisotropy are derived from the Laplace transform of the time-domain ones derived by Wang and Achenbach [30]. Applying the Laplace transform to the time-domain fundamental solutions yields the Laplace-domain ones as follows:

$$\hat{U}_{ij}(\mathbf{x}, \mathbf{y}, s) = \int_0^\infty U_{ij}(\mathbf{x}, \mathbf{y}, t) e^{-st} dt = \hat{U}_{ij}^S(\mathbf{x}, \mathbf{y}) + \hat{U}_{ij}^D(\mathbf{x}, \mathbf{y}, s) \quad (24)$$

where $\hat{U}_{ij}^S(\mathbf{x}, \mathbf{y})$ and $\hat{U}_{ij}^D(\mathbf{x}, \mathbf{y}, s)$ represent the static and dynamic parts of the fundamental solutions, respectively.

For 3-D problems, $\hat{U}_{ij}^S(\mathbf{x}, \mathbf{y})$ and $\hat{U}_{ij}^D(\mathbf{x}, \mathbf{y}, s)$ are expressed as follows:

$$\hat{U}_{ij}^S(\mathbf{x}, \mathbf{y}) = \frac{1}{8\pi^2 r} \int_{|\mathbf{n}|=1} \Gamma_{ij}^{-1}(\mathbf{n}) dL(\mathbf{n}), \quad (25)$$

$$\hat{U}_{ij}^D(\mathbf{x}, \mathbf{y}, s) = -\frac{1}{8\pi^2} \int_{|\mathbf{n}|=1} \sum_{m=1}^3 \frac{s_m d_i^m d_j^m}{\rho c_m^2} e^{-s_m |\mathbf{n} \cdot \mathbf{r}|} dL(\mathbf{n}) \quad (26)$$

where c_m and d_i^m are the phase velocity and the component of the polarization vector, respectively, which are functions of the propagation vector \mathbf{n} . In addition, $\mathbf{r} = \mathbf{x} - \mathbf{y}$, $r = |\mathbf{r}|$ and $s_m = s/c_m$. In Eq. (25), $\Gamma_{ij}(\mathbf{n})$ represents the Christoffel tensor given by

$$\Gamma_{ij}(\mathbf{n}) = C_{ipjq} n_p n_q. \quad (27)$$

The 3-D fundamental solutions involve the numerical integration over the unit sphere as shown in Fig. 2. In addition, the traction fundamental solution $\hat{W}_{ij}(\mathbf{x}, \mathbf{y}, s)$ is obtained using the relation

$$\hat{W}_{ij}(\mathbf{x}, \mathbf{y}, s) = -C_{jpqr} n_p(\mathbf{y}) \hat{U}_{iq,r}(\mathbf{x}, \mathbf{y}, s) \quad (28)$$

where $n_p(\mathbf{y})$ represents the unit normal vector on the boundary S .

For 2-D problems, the Laplace-domain fundamental solutions are expressed as follows:

$$\hat{U}_{ij}(\mathbf{x}, \mathbf{y}, s) = \frac{1}{8\pi^2} \int_{|\mathbf{n}|=1} \sum_{m=1}^3 \frac{d_i^m d_j^m}{\rho c_m^2} \Phi(\mathbf{n}, \mathbf{r}, s_m) dL(\mathbf{n}) \quad (29)$$

where

$$\Phi(\mathbf{n}, \mathbf{r}, s_m) = e^{s_m |\mathbf{n} \cdot \mathbf{r}|} E_1(s_m |\mathbf{n} \cdot \mathbf{r}|) + e^{-s_m |\mathbf{n} \cdot \mathbf{r}|} [E_1(-s_m |\mathbf{n} \cdot \mathbf{r}|) + i\pi]. \quad (30)$$

In Eq. (30), $E_1(z)$ represents the exponential integral [1]. As shown in Eq. (24), the 2-D fundamental solutions can be decomposed into static and dynamic parts using the following two relations. The first one is a series expansion of $E_1(z)$ as follows:

$$E_1(z) = -\gamma - \ln z - \sum_{n=1}^{\infty} \frac{(-1)^n z^n}{n \cdot n!} \quad (|\arg z| < \pi). \quad (31)$$

The other one is another form of the Christoffel tensor $\Gamma_{ij}(\mathbf{n})$ as

$$\Gamma_{ij}^{-1}(\mathbf{n}) = \sum_{m=1}^3 \frac{d_i^m d_j^m}{\rho c_m^2}. \quad (32)$$

Using Eqs. (31) and (32), the static and dynamic parts of the fundamental solutions can be obtained as follows:

$$\hat{U}_{ij}^S(\mathbf{x}, \mathbf{y}) = -\frac{1}{4\pi^2} \int_{|\mathbf{n}|=1} \Gamma_{ij}^{-1}(\mathbf{n}) \ln |\mathbf{n} \cdot \mathbf{r}| dL(\mathbf{n}), \quad (33)$$

$$\hat{U}_{ij}^D(\mathbf{x}, \mathbf{y}, s) = \frac{1}{8\pi^2} \int_{|\mathbf{n}|=1} \sum_{m=1}^3 \frac{d_i^m d_j^m}{\rho c_m^2} \Phi^D(\mathbf{n}, \mathbf{r}, s_m) dL(\mathbf{n}). \quad (34)$$

The function $\Phi^D(\mathbf{n}, \mathbf{r}, s)$ in Eq. (34) is given by

$$\Phi^D(\mathbf{n}, \mathbf{r}, s) = \Phi(\mathbf{n}, \mathbf{r}, s) + 2 \ln |\mathbf{n} \cdot \mathbf{r}|. \quad (35)$$

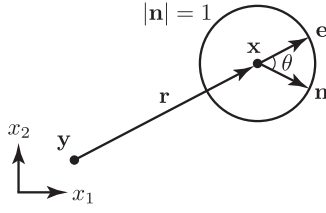


Fig. 3. Numerical integration over the unit circle.

The static part $\hat{U}_{ij}^S(\mathbf{x}, \mathbf{y})$ of Eq. (33) can be expressed in the closed form proposed by Wang [29], derived using a residue theorem as follows:

$$\hat{U}_{ij}^S(\mathbf{x}, \mathbf{y}) = \frac{1}{\pi} \text{Im} \left[\sum_{m=1}^3 \frac{A_{ij}(\eta_m)}{\partial_\eta D(\eta_m)} \ln(r_1 + r_2 \eta_m) \right] + R_{ij} \quad (36)$$

where

$$R_{ij} = -\frac{1}{\pi} \text{Im} \left[\sum_{m=1}^3 \frac{A_{ij}(\eta_m)}{\partial_\eta D(\eta_m)} \ln(\eta_m + i) \right]. \quad (37)$$

In Eqs. (36) and (37), ∂_η is given by $\partial_\eta = \partial/\partial\eta$, and the constant term R_{ij} is necessary to maintain the quiescent field ahead of the wave fronts generated by a point force and inessential in the elastostatic fundamental solution. In Eq. (36), $A_{ij}(\eta)$ and $D(\eta)$ represent the cofactor matrix and determinant of $\Gamma_{ij}(\mathbf{m})$, respectively, where $\mathbf{m} = \{1, \eta\}^T$. The superscript T denotes the transpose of a vector. Moreover, η_m are distinct roots of the following characteristic equation:

$$D(\eta_m) = 0, \quad \text{Im}[\eta_m] > 0 \quad (m = 1, 2, 3). \quad (38)$$

Note that the dynamic part of the 2-D fundamental solutions expressed by Eq. (34) involves the numerical integration over the unit circle as shown in Fig. 3. The corresponding traction fundamental solution $\hat{W}_{ij}(\mathbf{x}, \mathbf{y}, s)$ for 2-D problems can be obtained using the following relation:

$$\hat{W}_{ij}(\mathbf{x}, \mathbf{y}, s) = -C_{jaq\beta} n_\alpha(\mathbf{y}) \hat{U}_{iq,\beta}(\mathbf{x}, \mathbf{y}, s). \quad (39)$$

4. Numerical evaluation of the influence functions

The influence functions given by Eqs. (22) and (23) include Laplace-domain fundamental solutions for general anisotropic elastodynamics. These fundamental solutions given by Eqs. (25) and (26), and Eq. (34) involve the integration over the unit sphere and circle, respectively. In our proposed method, these integrations are numerically evaluated. However, numerical evaluation of these integrations is time-consuming. In this section, some numerical techniques for efficient calculation are introduced.

4.1. Numerical evaluation of the fundamental solutions

For 3-D problems, the numerical integration is implemented with respect to the azimuthal and polar angles, θ and ϕ , as shown in Fig. 2. Using the $(p+1)$ -point Gauss–Legendre rule for θ and the $(2p+1)$ -point trapezoidal rule for ϕ , the integration over the unit sphere is performed as follows:

$$\begin{aligned} \int_{|\mathbf{n}|=1} f(\mathbf{n}) dL(\mathbf{n}) &= \int_0^{2\pi} \int_0^\pi f(\phi, \theta) \sin \theta d\theta d\phi \\ &= \int_0^{2\pi} \int_{-1}^1 f(\phi, \cos^{-1}x) dx d\phi \\ &= \sum_{l=0}^{2p} \sum_{j=1}^{p+1} \eta_j^p f(\phi_j^p, \lambda_j^p) w_j^p \end{aligned} \quad (40)$$

where w_j^p and λ_j^p are the J -th weight and the arccosine of the J -th abscissa of the $(p+1)$ point Gauss–Legendre integration. In

addition, ϕ_l^p and η_l^p are expressed as

$$\phi_l^p = \frac{2\pi l}{2p+1}, \quad \eta_l^p = \frac{2\pi}{2p+1}. \quad (41)$$

For 2-D case, the unit circle is divided into n panels, each approximated by p -point Gauss–Legendre quadrature is applied to each panel. Then the integration over the unit circle is evaluated as follows:

$$\begin{aligned} \int_{|\mathbf{n}|=1} f(\mathbf{n}) dL(\mathbf{n}) &= \int_0^{2\pi} f(\theta) d\theta \\ &= \frac{\pi}{n} \sum_{l=1}^n \sum_{j=1}^p f(\lambda_{lj}^p) w_j^p \end{aligned} \quad (42)$$

where

$$\lambda_{lj}^p = \theta_{j-1} + \frac{\pi}{n}(1 + \lambda_j^p), \quad \theta_j = \frac{2\pi j}{n}. \quad (43)$$

In the numerical examples presented later, the parameters are set to be $p=150$ for the 3-D problem, and $n=8$ and $p=16$ for the 2-D problem.

4.2. Acceleration of numerical computation for the influence functions

Numerical computation of the influence functions as shown in Eqs. (22) and (23) requires much computational time. However, the computation of these functions can be accelerated using the following three techniques.

Clearly, the influence functions defined in Eqs. (22) and (23) are of the same form as a discrete Fourier transform (DFT). Therefore, these influence functions can quickly be evaluated by means of fast Fourier transform (FFT).

The second technique involves the complex conjugate of the influence functions. The distribution of $\gamma(z)$ on the complex plane defined in Eq. (20) is shown in Fig. 4, for the CQM parameters $\mathcal{R}=0.9$, $L=64$ and $k=2$ in Eq. (20). As shown in this figure, the following symmetric relation about $\gamma(z)$ is obtained as

$$\gamma(z_{L-k}) = \overline{\gamma(z_k)} \quad (k = 1, 2, \dots, L/2 - 1) \quad (44)$$

where $\overline{(\cdot)}$ represents the complex conjugate. Taking into account this symmetric property about the real axis as shown in Fig. 4, the following equation can be obtained as

$$\hat{U}_{ij}(\mathbf{x}, \mathbf{y}, s_{L-k}) = \overline{\hat{U}_{ij}(\mathbf{x}, \mathbf{y}, s_k)} \quad (k = 1, 2, \dots, L/2 - 1). \quad (45)$$

Therefore, it is necessary to compute the boundary integrations for the fundamental solutions $\hat{U}_{ij}(\mathbf{x}, \mathbf{y}, s_l)$ and its double layer kernel

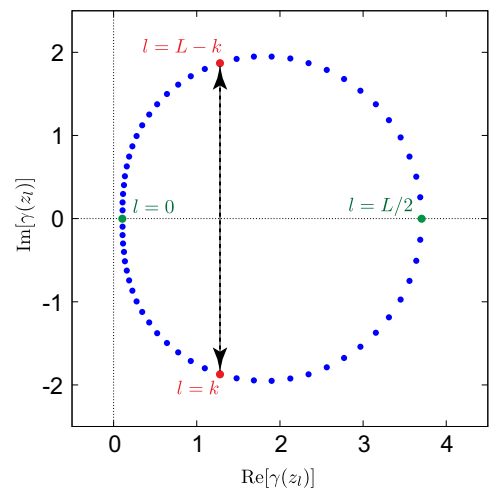


Fig. 4. Distribution of $\gamma(z)$ on the complex plane.

$\hat{W}_{ij}(\mathbf{x}, \mathbf{y}, s_l)$, only for $l = 0, 1, \dots, L/2$. The remaining calculations for $l = L/2 + 1, L/2 + 2, \dots, L - 1$ can be evaluated using the symmetric property defined in Eq. (45).

The final means of increasing the processing speed is to truncate the computation of the fundamental solutions. For instance, negligibly small values of the fundamental solutions are excluded from their integration process. To this end, it is important to investigate the asymptotic behavior of the fundamental solutions.

For 3-D case, as shown in Eq. (26), the integral kernel of the dynamic part of the fundamental solutions $\hat{U}_{ij}^D(\mathbf{x}, \mathbf{y}, s_l)$ is

$$\frac{s_m d_i^m d_j^m}{\rho c_m^2} e^{-s_m |\mathbf{n} \cdot \mathbf{r}|} \quad (46)$$

This integral kernel includes $\exp(-s_m |\mathbf{n} \cdot \mathbf{r}|)$ which tends to zero for a large argument $s_m |\mathbf{n} \cdot \mathbf{r}|$. Therefore, considering $|s_m| \rightarrow \infty$ or $r \rightarrow \infty$, Eq. (46) can be rewritten as

$$\frac{s_m d_i^m d_j^m}{\rho c_m^2} e^{-s_m |\mathbf{n} \cdot \mathbf{r}|} \propto e^{-\text{Re}[s_m] |\mathbf{n} \cdot \mathbf{r}|} \quad (47)$$

Therefore, the truncation condition for 3-D case is derived from the relation, $\mathbf{r} = r\mathbf{e}$ (see Fig. 2) as follows:

$$e^{-\text{Re}[s_m] r} < 10^{-\beta} \quad \text{or} \quad r > \frac{\beta \ln 10}{\text{Re}[s_m]} \quad (48)$$

where β is the truncation parameter. If the truncation condition defined in Eq. (48) is satisfied, $\hat{U}_{ij}^D(\mathbf{x}, \mathbf{y}, s_l)$ is neglected and the fundamental solutions (24) are approximated as

$$\hat{U}_{ij}(\mathbf{x}, \mathbf{y}, s) \simeq \hat{U}_{ij}^S(\mathbf{x}, \mathbf{y}). \quad (49)$$

The same procedure can be applied to the 2-D problem. Therefore, considering the asymptotic behavior of $\hat{U}_{ij}(\mathbf{x}, \mathbf{y}, s)$ given by Eq. (29) ($|s_m| \rightarrow \infty$ or $r \rightarrow \infty$), the exponential integral is expanded as follows [1]:

$$E_1(z) \sim \frac{e^{-z}}{z} \left(1 - \frac{1}{z} + \frac{2}{z^2} - \frac{6}{z^3} + \dots \right). \quad (50)$$

Using Eq. (50), the integral kernel of Eq. (29) can be approximated as follows:

$$\frac{d_i^m d_j^m}{\rho c_m^2} \phi(\mathbf{n}, \mathbf{r}, s_m) \propto e^{-\text{Re}[s_m] |\mathbf{n} \cdot \mathbf{r}|} \quad (51)$$

Therefore, the truncation condition defined in Eq. (48) is applicable to Eq. (51). Indeed, if the truncation condition expressed by (48) is satisfied, the fundamental solutions $\hat{U}_{ij}(\mathbf{x}, \mathbf{y}, s)$ are approximated as follows:

$$\hat{U}_{ij}(\mathbf{x}, \mathbf{y}, s) \simeq 0. \quad (52)$$

Since this truncation depends strongly on r , the approximation given by Eq. (52) represents neglect of waves propagating from far-field ($r \rightarrow \infty$). This truncation is applied only to computation of influence functions in which the relation between collocation points and boundary elements can be considered to far-field. A different approach to efficient computation has been proposed by Hackbusch and Kress [12]. The approach is for fast evaluation of the influence functions (i.e. integrations on the boundary elements) and based on the distance from the source point \mathbf{y} to the observation point \mathbf{x} .

Three techniques introduced herein effectively accelerate the numerical computation of the influence functions given by Eqs. (22) and (23). The first and second techniques can be applied without difficulty. However, the third one involves the empirical truncation parameter β which can be determined subject to numerical error constrains before numerical implementation.

5. Numerical examples

In this section, some numerical examples, which are wave scattering problems by a spherical cavity in 3-D case and a circular one in 2-D case, are presented. First, the accuracy of our proposed method in solving 2-D and 3-D problems is confirmed. Next, for 3-D case, the computational efficiency is evaluated using parallelization techniques. Finally, numerical results for elastic wave scattering by a cavity are shown. In particular, three types of anisotropic solids are considered in 2-D problems.

Spherical and circular cavities are divided into 512 and 32 boundary elements, respectively. A fine mesh is required for accurate computation of the waves propagating along the surface of spherical and circular cavities. Moreover, the QM parameters $c = 1.0 \times 10^{-10}$ in Eq. (19) and $k=2$ in Eq. (20) are considered.

5.1. Accuracy of the proposed method

The 3-D scattering problem of an incident plane P-wave hitting a spherical cavity with radius a in an infinite domain, as shown in Fig. 5, is solved by the proposed method to verify the computational accuracy.

The formulation for 3-D general anisotropy proposed herein involves an elastic constant C_{ijkl} , as shown in Eq. (27). If the isotropic elastic constants are substituted into the coefficients C_{ijkl} of each derived equation, we can solve the isotropic problem and compare with the “reference solutions,” which are obtained by inversely transforming the analytical solutions in the frequency domain [21].

The number of total time steps $N (=L)$ is 32, and the time increment is given by $c_L \Delta t / a = 0.08$ where c_L is the phase velocity of an incident P-wave. Poisson’s ratio ν of elastic solid is 0.25. The incident wave is a plane longitudinal wave given by

$$u_i^{\text{in}}(\mathbf{x}, t) = \delta_{i1} \frac{\sigma_0 a}{\rho c_L^2} h_L H(h_L), \quad h_L = \frac{c_L t}{a} - \frac{x_1 + a}{a} \quad (53)$$

where σ_0 is the stress amplitude. In addition, $H(\cdot)$ and δ_{ij} represent Heaviside function and the Kronecker delta, respectively.

Fig. 6 shows the time variations of the total displacements at points A, B and C in Fig. 5. In Fig. 6, the circles and solid lines show the total displacements computed by our proposed method and the reference solutions, respectively. As seen in Fig. 6, the results obtained by our proposed method are in good agreement with the reference solutions. Therefore, it can be said that the validity of the formulation is confirmed for the 3-D case.

In the same way, the 2-D elastic wave scattering problem is solved by the proposed method. The analytical model is a circular cavity of radius a , as shown in Fig. 7. The number of total time steps $N (=L)$ is 128. In addition, the time increment Δt is given by $c_L \Delta t / a = 0.125$. The incident wave is a plane longitudinal wave expressed by Eq. (53). The time variations of the total displacements at points A, B and C in Fig. 7 are shown in Fig. 8. Our numerical results (colored circles) agree well with the 2-D reference solutions (colored solid lines). Thus, the proposed method was validated in both 2-D and 3-D cases.

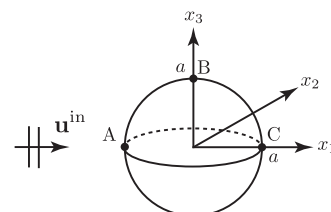


Fig. 5. Analytical model in the 3-D infinite domain.

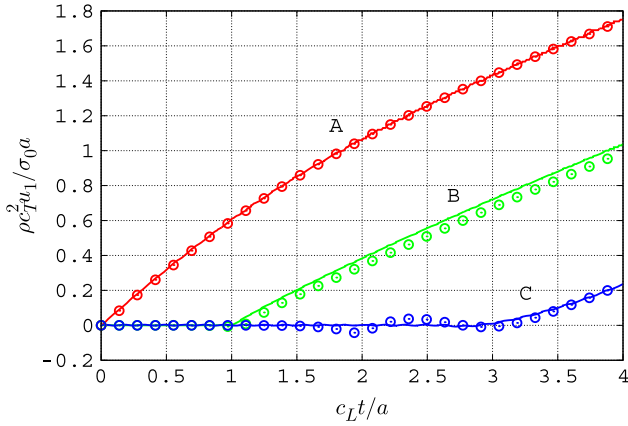


Fig. 6. Time variations of the total displacements at points A, B and C in Fig. 5.

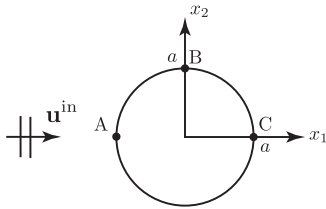


Fig. 7. Analytical model in the 2-D infinite domain.

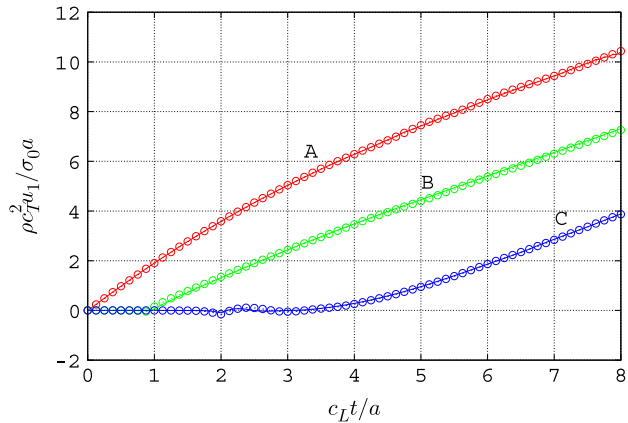


Fig. 8. Time variations of the total displacements at points A, B and C in Fig. 7 (Section 5.1). (For interpretation of the references to color in this figure caption, the reader is referred to the web version of this paper.)

5.2. Influence of truncation in computation of the fundamental solutions

In this section, the influence of truncation for computation of the fundamental solutions, described in Section 4.2, is verified by demonstrating numerical results obtained with different values of the truncation parameter β in Eq. (48). The numerical model is the 2-D elastic wave scattering problem as shown in Fig. 7. It is assumed that the medium is an isotropic elastic solid with Poisson's ratio $\nu=0.25$, and the incident wave is a plane longitudinal wave given by

$$u_i^{in}(\mathbf{x}, t) = U_0 d_i \frac{1}{2} [1 - \cos(2\pi h_L)] H(h_L) \tag{54}$$

where

$$h_L = \frac{c_L t}{a} - \frac{x_1 + a}{a}. \tag{55}$$

In Eq. (54), U_0 and d_i represent the amplitude and polarization vector of the incident wave, respectively. In addition, c_L is the phase velocity of the longitudinal wave. Total number of time step is set to $N_t=64$. The time increment is given by $c_T \Delta t / a = 0.029$ where c_T represents wave velocity of the transverse wave.

Fig. 9 shows time variations of total displacements at points A, B and C in Fig. 7. The truncation parameter β is set to 1, 2, 5, 10 and 20, and s_m in Eq. (48) is chosen as $s_m = s / c_L$. Note that the truncation parameter $\beta = \infty$ means that the truncation has not been applied. From Fig. 9, the total displacements with $\beta=5, 10$ and 20 are good agreement with the displacement without truncation ($\beta = \infty$) at all three points. Therefore, the truncation parameter with $\beta \geq 5$ is adequate for 2-D wave scattering analyses. Other truncation parameters should be selected for 3-D problems. Fig. 10 shows the relation between computational time and truncation parameter β . The computational time using $\beta=5$ is only 40% of the analysis without truncation ($\beta = \infty$). Our proposed truncation is powerful for reducing computational time. When anisotropic solids are considered, c^{\max} should be set to the phase velocity of quasi-P wave.

5.3. Computational efficiency of the proposed method

As mentioned before, the fundamental solutions in 3-D general anisotropy involve integration over the unit sphere and its

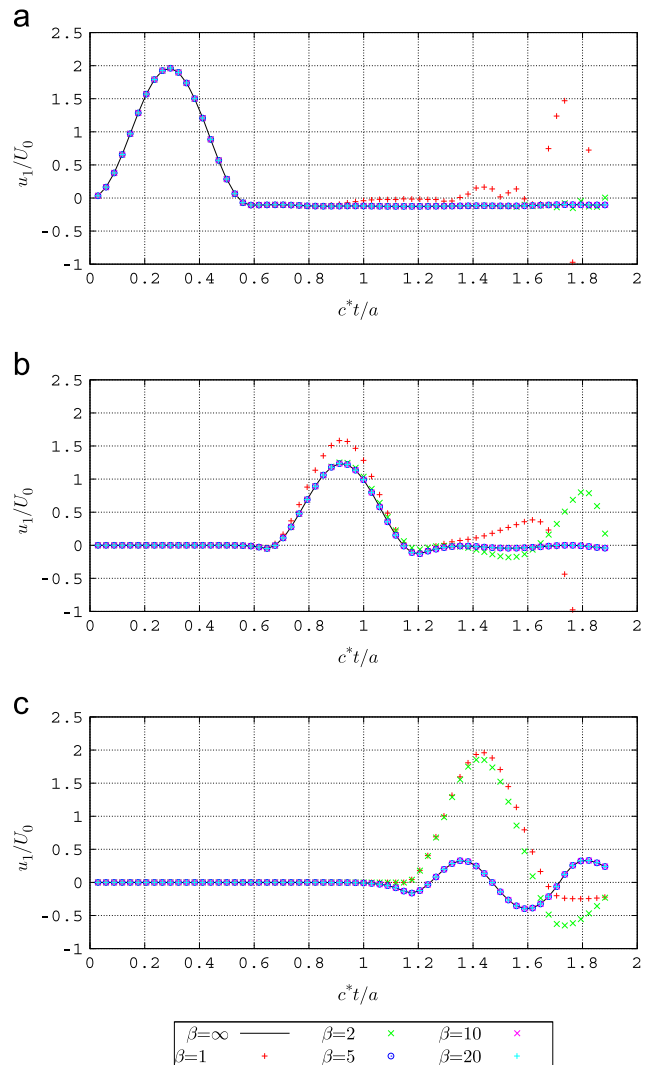


Fig. 9. Time variations of the total displacements at points A, B and C in Fig. 7 (Section 5.2).

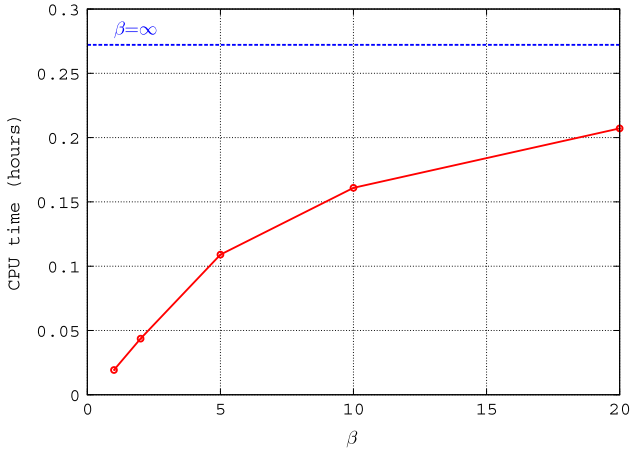


Fig. 10. Relation between computational time and truncation parameter β .

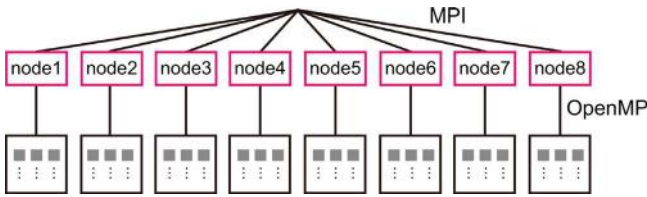


Fig. 11. Schematic diagram of the hybrid parallelization with MPI and OpenMP.

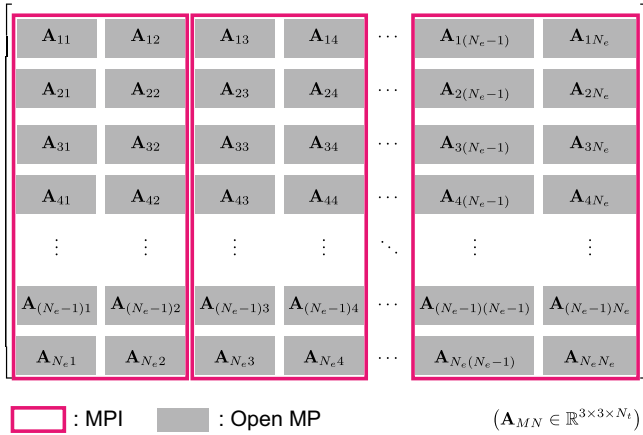


Fig. 12. Parallel memory allocation for the influence matrix $A_{MN}^{(m)}$.

computation is very time-consuming. Therefore, in this section, the computational efficiency of the formulation for 3-D problem is confirmed by resolving the problem outlined in Section 5.1 using a hybrid parallelization with MPI and OpenMP.

A schematic diagram of the hybrid parallelization is shown in Fig. 11. In this paper, eight nodes are used in the MPI process, and the number of threads per node (i.e. OpenMP parallelization) is 1, 6, 12 and 24. Fig. 12 shows the assignment of the parallelization corresponding to the components of the influence matrix in Eq. (21). The matrix shown in Fig. 12 consists of the influence functions A_{MN} given by Eq. (22). In addition, the following MPI-OpenMP relation makes it possible to obtain a good speed-up:

$$\frac{N_e^2}{pq} \in \mathbb{N} \quad (= 1, 2, 3, \dots) \quad (56)$$

In Eq. (56), p represents the number of nodes by MPI process, and q is the number of threads by OpenMP. Numerical computation based on the relation that does not meet Eq. (56) generates nodes

Table 1 Relationship between the computational time and the number of total threads used in this analysis.

MPI	OpenMP	The number of total threads	CPU time (h)
8	1	8	22.6
8	6	48	7.5
8	12	96	1.9
8	24	192	1.6

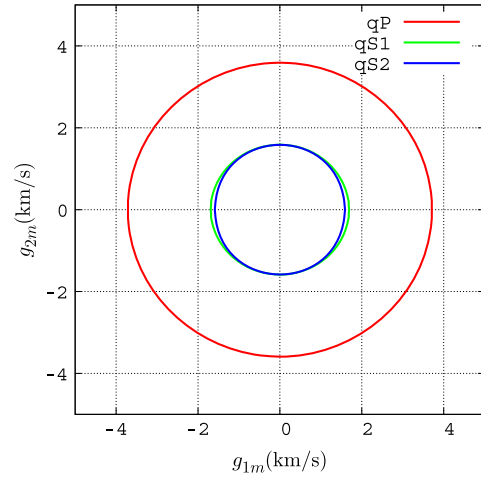


Fig. 13. Group velocity curves (PZT, x_1-x_2 section).

and slave threads which are only waiting for joining back into the master thread.

Table 1 shows the relationship between the computational time and the number of total threads used in this analysis. TSUBAME 2.0, which is a supercomputer at Tokyo Institute of Technology, is used for the computation. From these results, it can be observed that the required computational time is drastically decreased by using the hybrid parallelization. From the practical point of view, however, the time-domain analysis for 3-D general anisotropy remains time-consuming.

5.4. Elastic wave scattering analysis by a cavity in anisotropic solids

In this section, the results of 2-D elastic wave scattering by a cavity in anisotropic solids are demonstrated. Three types of anisotropic solids, namely, transversely isotropic, orthotropic and monoclinic materials, are considered in the analysis.

In the following numerical results, the number of total time steps N_t is set to be $N_t = L = 32$. The incident wave is the plane quasi-P wave given by Eqs. (54) and (55). Phase velocity and polarization vector of the quasi-P wave should be substituted into c_P and d_i (i.e. $c_P := c_{qP}$ and $d_i := d_i^{qP}$) in these equations. Note that both phase velocity c_{qP} and polarization vector d_i depend on the type of anisotropic solids. To improve the computational efficiency, the computations are parallelized by 24 OpenMP threads.

Numerical simulations of scattering in a transversely isotropic solid are conducted for the PZT (lead zirconate titanate). The density of PZT is 7800 kg/m^3 , and the elastic tensor components based on the Voigt notation C_{ij} (GPa) [11] are

$$C_{ij} = \begin{bmatrix} 107.6 & 63.9 & 63.1 & 0 & 0 & 0 \\ & 100.4 & 63.9 & 0 & 0 & 0 \\ & & 107.6 & 0 & 0 & 0 \\ & & & 19.6 & 0 & 0 \\ \text{Sym.} & & & & 22.2 & 0 \\ & & & & & 19.6 \end{bmatrix} \quad (57)$$

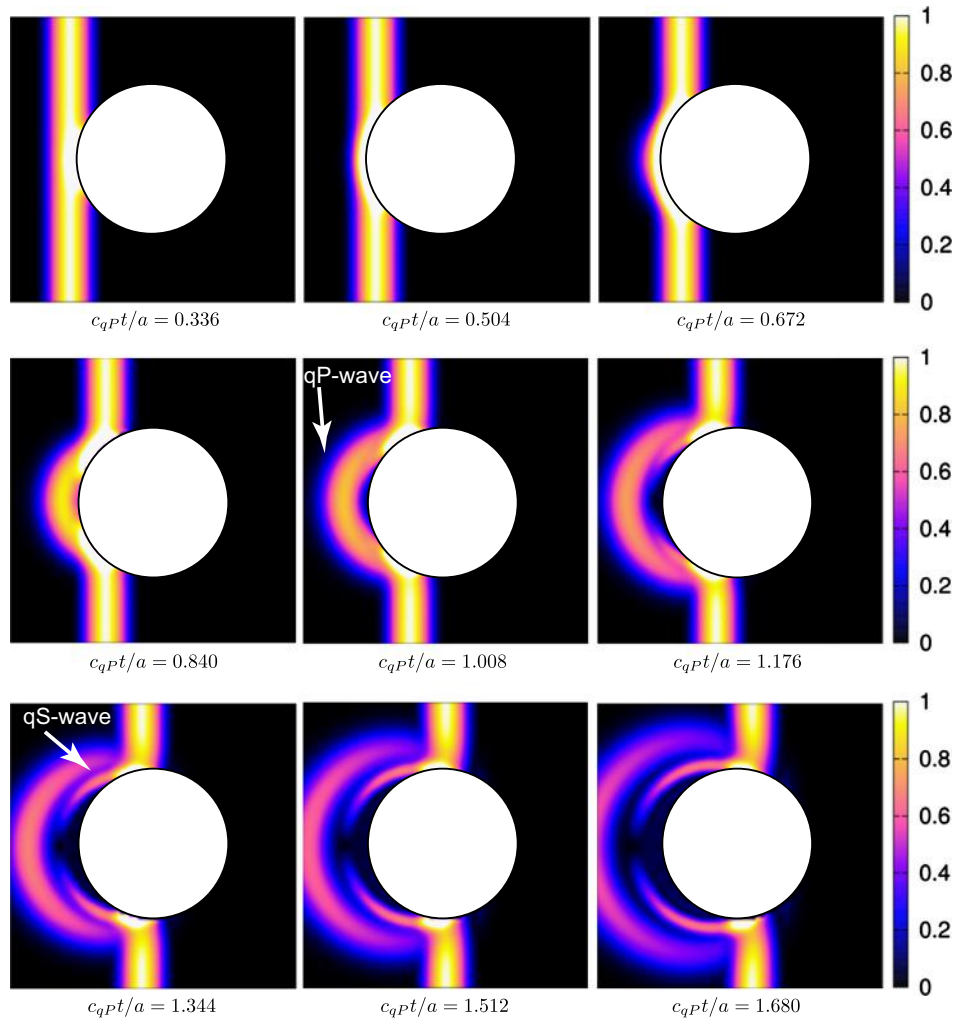


Fig. 14. Time histories of the total wave fields around a cavity at several times (PZT, x_1 - x_2 section).

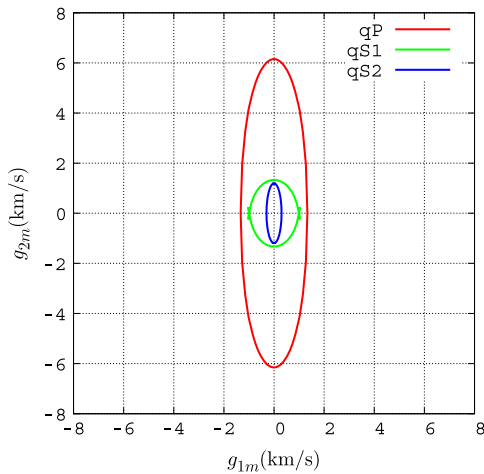


Fig. 15. Group velocity curves (spruce, x_1 - x_2 section).

The phase velocity of the quasi-P wave propagating parallel to the x_1 -direction is 3700 m/s, and the polarization vector of the wave is $\mathbf{d} = \{1, 0\}^T$. The time increment is $c_{qP}\Delta t/a = 0.056$. The group velocity curves of PZT in the x_1 - x_2 section are shown in Fig. 13. From this figure, it can be observed that the shapes of the curves are almost circles. Fig. 14 shows time histories of the total wave fields, $|\mathbf{u}|/U_0$, at several times. The results show clear wave fronts

of scattered quasi-P and quasi-S1 waves propagating with rotationally symmetric wave fronts that are similar to the group velocity curves in Fig. 13.

Numerical simulations are then conducted for an orthotropic material, namely, spruce. The density of spruce is 430 kg/m^3 , and its elastic tensor components C_{IJ} (GPa) [11] are

$$C_{IJ} = \begin{bmatrix} 0.44 & 0.32 & 0.19 & 0 & 0 & 0 \\ & 16.27 & 0.45 & 0 & 0 & 0 \\ & & 0.78 & 0 & 0 & 0 \\ & & & 0.61 & 0 & 0 \\ \text{Sym.} & & & & 0.039 & 0 \\ & & & & & 0.76 \end{bmatrix}. \quad (58)$$

The phase velocity of the quasi-P wave propagating parallel to the x_1 -direction is $c_{qP} = 1300 \text{ m/s}$. The polarization vector of the wave is given as $\mathbf{d} = \{0, 1\}^T$. Moreover, the time increment $c_{qP}\Delta t/a = 0.098$ is considered in this analysis. Fig. 15 shows the group velocity curves of spruce in the x_1 - x_2 cross-section. From this figure, it can be observed that the group velocity of quasi-P waves propagating in the x_2 -direction is faster than that in the x_1 -direction. The time histories of the total wave fields, $|\mathbf{u}|/U_0$, at several times are shown in Fig. 16. This figure shows that the incident wave is scattered and the shape of the scattered quasi-P wave is consistent with the group velocity curves of Fig. 15.

Finally, simulations are performed for a monoclinic material, graphite-epoxy. The density of graphite-epoxy is 1600 kg/m^3 , and

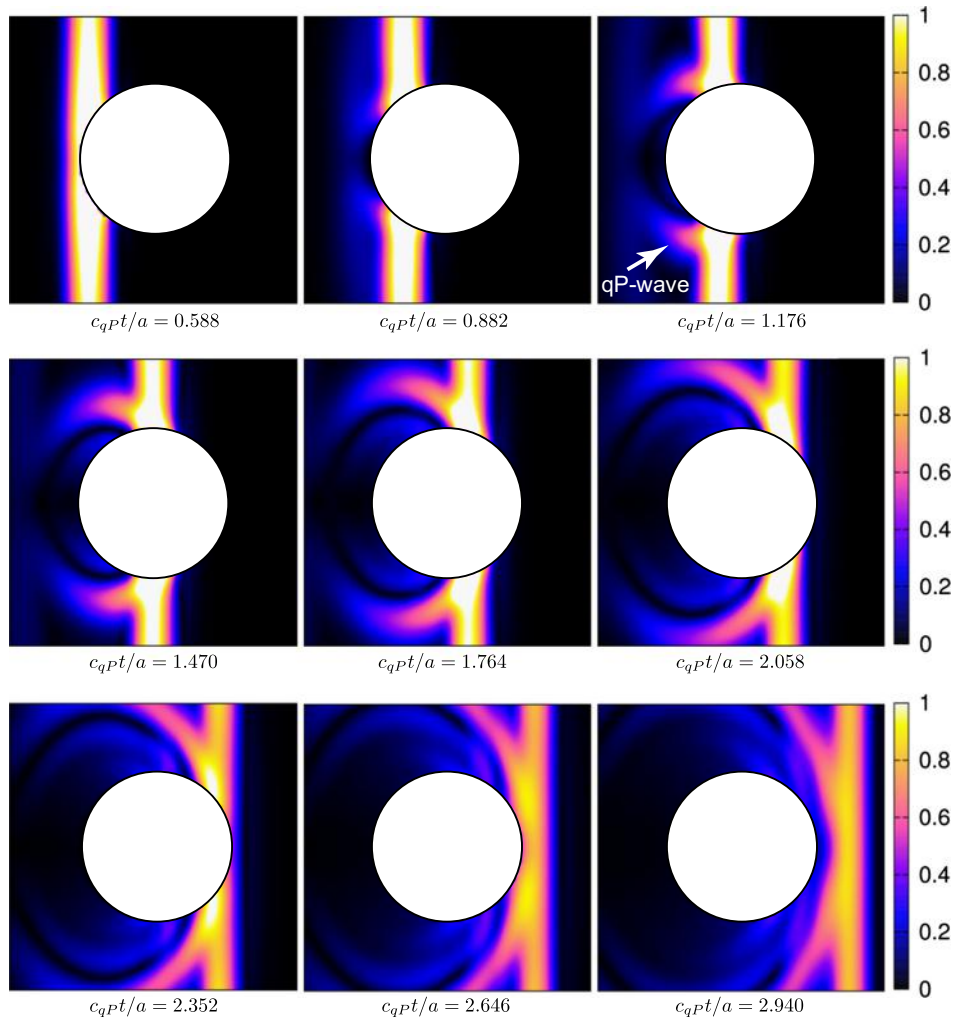


Fig. 16. Time histories of the total wave fields around a cavity at several times (spruce, x_1 - x_2 section).

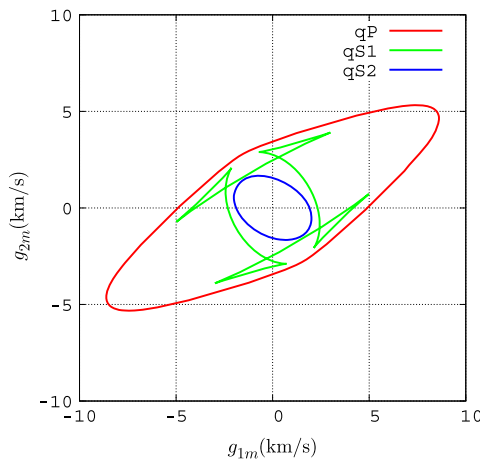


Fig. 17. Group velocity curves (graphite-epoxy, x_1 - x_2 section).

The phase velocity of the quasi-P wave propagating parallel to the x_1 -direction c_{qP} is 8600 m/s, and the polarization vector of the wave is $\mathbf{d} = \{0.88, -0.46\}^T$. In addition, the time increment is $c_{qP}\Delta t/a = 0.129$. The group velocity curves of graphite-epoxy in the x_1 - x_2 section are shown in Fig. 17. As seen in Fig. 17, the group velocity curve of quasi-S1 wave is somewhat erratic. The time histories of the total wave fields, $|\mathbf{u}|/U_0$, at several times are shown in Fig. 18. The wave fronts of the scattered waves concord with the group velocity curves.

6. Conclusions

In this paper, CQ-BEMs for 2-D and 3-D elastodynamic analyses of general anisotropy were presented. Our proposed method adopted the CQM and the collocation method for time and spatial discretization, respectively. The Laplace-domain fundamental solutions were required for the computation of the influence functions, which were derived from the time-domain fundamental solutions proposed by Wang and Achenbach [30]. For the 3-D case, numerical integration over the unit sphere was performed for both static and dynamic parts. On the other hand, for the 2-D case, dynamic part only was numerically integrated, while the static part was calculated analytically. In addition, some numerical techniques for the efficient computation of the influence functions were presented.

the elastic tensor components C_{IJ} (GPa) [11] are

$$C_{IJ} = \begin{bmatrix} 95.5 & 28.9 & 4.03 & 0 & 0 & 44.7 \\ 25.9 & 4.65 & 0 & 0 & 0 & 15.6 \\ & 16.3 & 0 & 0 & 0 & 0.54 \\ & & 4.4 & -1.78 & 0 & \\ \text{Sym.} & & & 6.45 & 0 & \\ & & & & & 32.7 \end{bmatrix} \quad (59)$$

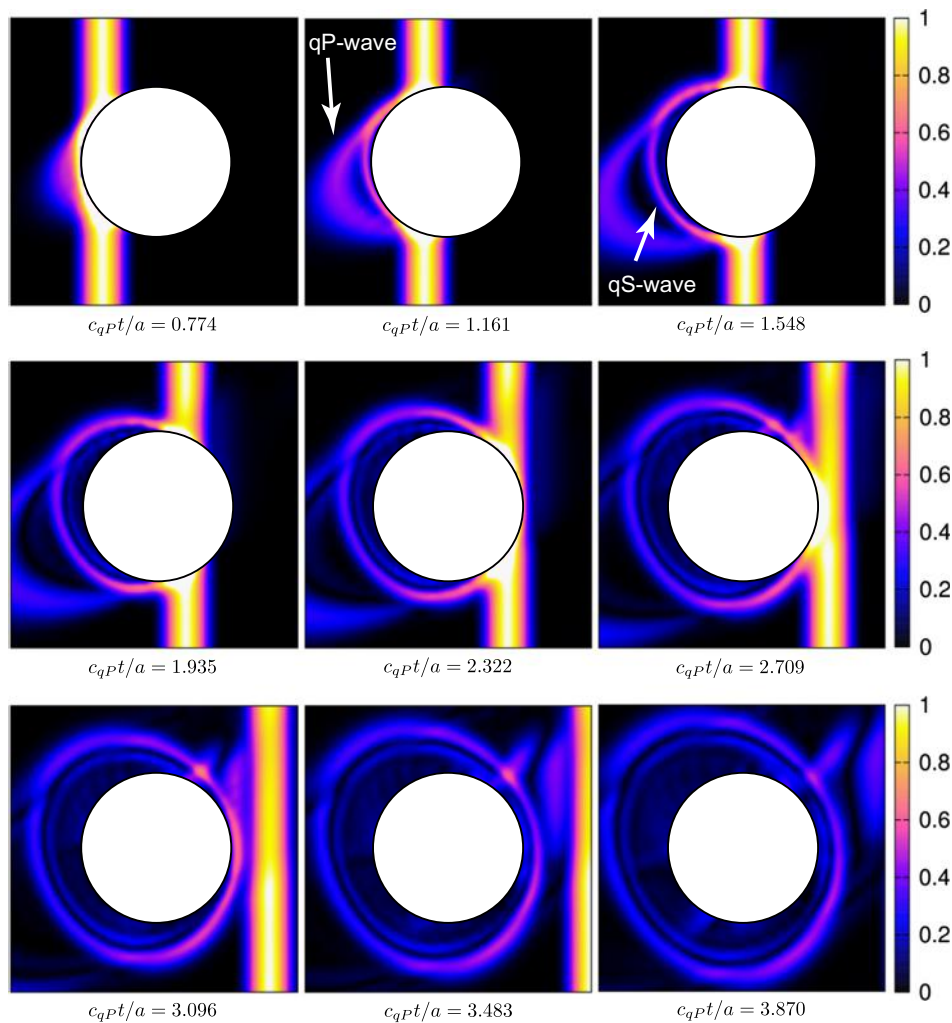


Fig. 18. Time histories of the total wave fields around a cavity at several times (graphite-epoxy, x_1 - x_2 section).

To verify the proposed method, wave scattering problems in general anisotropic solids were demonstrated for both 2-D and 3-D cases. The accuracy of our proposed method was confirmed by comparing our results with the semi-analytical solutions in the cases of isotropic solids. To investigate the computational efficiency in 3-D cases, CPU times were compared by using the hybrid parallel calculations with different numbers of threads in MPI and OpenMP. Finally, the results of wave scattering analysis for the 2-D problems were presented for three anisotropic solids.

Both 2-D and 3-D analyses required much computational time and memory. A future task is to improve our proposed method further in conjunction with FMM or adaptive cross approximation (ACA). In addition, although the superior time stability of the CQ-BEM compared with the conventional time-domain BEM is well known, a mesh-sensitivity study of the CQ-BEM is required. In near future, the CQ-BEM for solving wave scattering in general anisotropic fluid-saturated porous solids will be developed.

References

- [1] Abramowitz M, Stegun IA. Handbook of mathematical functions with formulas, graphs, and mathematical tables. New York: Dover Publications, Inc.; 1965.
- [2] Aimi A, Diligenti M. A new space-time energetic formulation for wave propagation analysis in layered media by BEMs. *Int J Numer Methods Eng* 2008;75:1102–32.
- [3] Albuquerque EL, Sollero P, Aliabadi MH. The boundary element method applied to time dependent problems in anisotropic materials. *Int J Solid Struct* 2002;39:1405–22.
- [4] Antes H. A boundary element procedure for transient wave propagations in two-dimensional isotropic elastic media. *Finite Elem Anal Des* 1985;1:313–22.
- [5] Banjai L, Messer M, Schanz M. Runge–Kutta convolution quadrature for the boundary element method. *Comput Methods Appl Mech Eng* 2012;245–246:90–101.
- [6] Denda M, Wang CY, Yong YC. 2D time-harmonic BEM for solids of general anisotropy with application to eigenvalue problems. *J Sound Vib* 2003;261:247–76.
- [7] Denda M, Marante ME. Mixed mode BEM analysis of multiple curvilinear cracks in the general anisotropic solids by the crack tip singular element. *Int J Solid Struct* 2004;41:1473–89.
- [8] Domínguez J. Boundary elements in dynamics. Southampton: Computational Mechanics Publications; 1993.
- [9] Furukawa A, Saitoh T, Hirose S. Two-dimensional elastic wave scattering analysis by a crack for general anisotropy using convolution quadrature boundary element method. In: 4th International conference on computational methods, ICCM2012, Gold Coast, Australia, 25–28 November 2012.
- [10] García-Sánchez F, Zhang Ch. A comparative study of three BEM for transient dynamic crack analysis of 2-D anisotropic solids. *Comput Mech* 2007;40:753–69.
- [11] Gaul L, Kogl M, Wagner M. Boundary element method for engineers and scientists. New York: Springer; 2002.
- [12] Hackbusch W, Kress W. Sparse convolution quadrature for time domain boundary integral formulations of the wave equation. *IMA J Numer Anal* 2008;29:158–79.
- [13] Hirose S. Boundary integral equation method for transient analysis of 3-D cavities and inclusions. *Eng Anal Bound Elem* 1991;8:146–53.
- [14] Lubich C. Convolution quadrature and discretized operational calculus I. *Numer Math* 1988;52:129–45.

- [15] Lubich C. Convolution quadrature and discretized operational calculus II. *Numer Math* 1988;52:413–25.
- [16] Lubich C, Schneider R. Time discretization of parabolic boundary integral equations. *Numer Math* 1992;63:455–81.
- [17] Lubich C. On the multistep discretization of linear initial-boundary value problems and their boundary integral equations. *Numer Math* 1994;67:365–89.
- [18] Mansur WJ, Brebbia CA. Transient elastodynamics using a time-stepping technique. In: Brebbia CA, Futagami T, Tanaka M, editors. *Boundary elements*. Southampton: Berlin and CML Publications; 1983.
- [19] Pan E. A general boundary element analysis of 2-D linear elastic fracture mechanics. *Int J Fract* 1997;88:41–59.
- [20] Pan E, Yuan FG. Boundary element analysis of three-dimensional cracks in anisotropic solids. *Int J Numer Methods Eng* 2000;48:211–37.
- [21] Pao Y-H, Mow CC. *Diffraction of elastic waves and dynamic stress concentrations*. New York: Crane and Russak; 1973.
- [22] Schanz M, Antes H. Application of 'Operational quadrature methods' in time domain boundary element method. *Meccanica* 1997;32:179–86.
- [23] Schanz M. A boundary element formulation in time domain for viscoelastic solids. *Commun Numer Methods Eng* 1999;15:799–809.
- [24] Schanz M. Application of 3D time domain boundary element formulation to wave propagation in poroelastic solids. *Eng Anal Bound Elem* 2001;25:367–76.
- [25] Sollero P, Aliabadi MH. Anisotropic analysis of cracks in composite laminates using dual boundary element method. *Compos Struct* 1995;31:229–33.
- [26] Takahashi T, Nishimura N, Kobayashi S. A fast BIEM for three-dimensional elastodynamics in time domain. *Eng Anal Bound Elem* 2003;27:491–506.
- [27] Tan A, Hirose S, Zhang Ch, Wang C-Y. A time-domain BEM for transient wave scattering analysis by a crack in anisotropic solids. *Eng Anal Bound Elem* 2005;29:610–23.
- [28] Ting TCT. *Anisotropic elasticity, theory and applications*. New York: Oxford University Press; 1996.
- [29] Wang C-Y. Two-dimensional elastostatic Green's functions for general anisotropic solids and generalization of Stroh's formalism. *Int J Solid Struct* 1994;31:2591–7.
- [30] Wang C-Y, Achenbach JD. Elastodynamic fundamental solutions for anisotropic solids. *Geophys J Int* 1994;118:384–92.
- [31] Wang C-Y, Achenbach JD, Hirose S. Two-dimensional time domain BEM for scattering of elastic waves in solids of general anisotropy. *Int J Solid Struct* 1996;33:3843–64.
- [32] Wünsche M, Zhang Ch, Kuna M, Hirose S, Sladek J, Sladek V. A hypersingular time-domain BEM for 2D dynamic crack analysis in anisotropic solids. *Int J Numer Methods Eng* 2009;78:127–50.
- [33] Zhang Ch. Transient elastodynamic antiplane crack analysis of anisotropic solids. *Int J Solid Struct* 2000;37:6107–30.